

Self-excited oscillations in three-dimensional collapsible tubes: simulating their onset and large-amplitude oscillations

MATTHIAS HEIL[†] AND JONATHAN BOYLE[‡]

School of Mathematics, University of Manchester, Oxford Road, Manchester M13 9PL, UK

(Received 15 September 2009; revised 5 January 2010; accepted 6 January 2010;
first published online 13 April 2010)

We employ numerical simulations to explore the development of flow-induced self-excited oscillations in three-dimensional collapsible tubes which are subject to boundary conditions (flow rate prescribed at the outflow boundary) that encourage the development of high-frequency oscillations via an instability mechanism originally proposed by Jensen & Heil (*J. Fluid Mech.*, vol. 481, 2003, p. 235). The simulations show that self-excited oscillations tend to arise preferentially from steady equilibrium configurations in which the tube is buckled non-axisymmetrically. We follow the growing oscillations into the large-amplitude regime and show that short tubes tend to approach an approximately axisymmetric equilibrium configuration in which the oscillations decay, whereas sufficiently long tubes develop sustained large-amplitude limit-cycle oscillations. The period of the oscillations and the critical Reynolds number beyond which their amplitude grows are found to be in good agreement with theoretical scaling estimates.

1. Introduction

The Starling resistor is an experimental device for the study of flows in collapsible tubes. It was originally developed by Knowlton & Starling (1912) to allow the adjustment of the arterial resistance in experimental studies of the mammalian heart but has since become a popular device for the study of a wide variety of physiological fluid–structure interaction problems. In the typical experimental set-up, sketched in figure 1, a thin-walled elastic tube is mounted on two rigid tubes and viscous fluid is driven through the elastic segment, either by an imposed pressure drop or by a volumetric pump. The elastic tube is surrounded by a pressure chamber which allows the external pressure p_{ext}^* to be controlled independently of the fluid pressure.

If the transmural pressure (the difference between the external and internal pressure) exceeds a certain threshold, the initially axisymmetric elastic tube tends to buckle non-axisymmetrically. Once buckled, the tube is very flexible and even small changes in the fluid pressure can induce large changes in the wall shape, resulting in strong fluid–structure interaction. This can have a strong effect on the system's pressure–flow relationships. For instance, depending on the boundary conditions, the system

[†] Email address for correspondence: M.Heil@maths.man.ac.uk

[‡] Present address: Research Computing Services, University of Manchester, Oxford Road, Manchester M13 9PL, UK

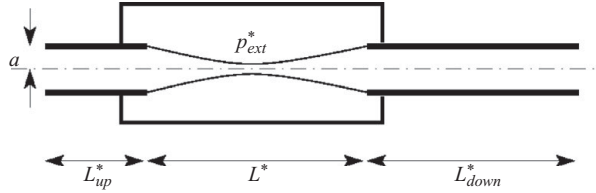


FIGURE 1. Sketch of the Starling resistor, a thin-walled elastic tube, mounted on two rigid tubes and enclosed in a pressure chamber.

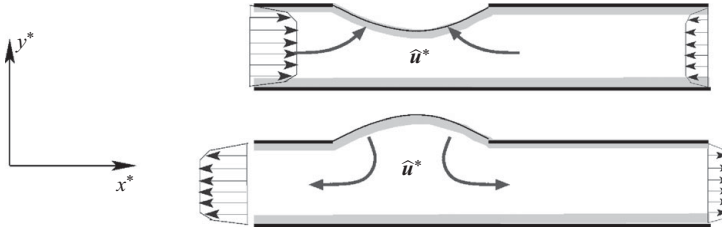


FIGURE 2. Sketch of the sloshing flows generated by the oscillatory wall motion in the two-dimensional collapsible channel analysed by Jensen & Heil (2003). The sloshing flow has an inviscid core region, with Stokes layers near the walls.

may display pressure-drop or flow-rate limitation. The latter is observed in a variety of physiological fluid–structure interaction problems, e.g. during forced expiration.

The most intriguing feature of the system is its propensity to develop sustained large-amplitude self-excited oscillations when the flow rate exceeds a critical value, again mirroring the behaviour observed in many physiological flow problems, such as the occurrence of wheezing during forced expiration, or the development of Korotkoff sounds during sphygmomanometry. We refer to Grotberg & Jensen (2004) for a more detailed discussion of physiological applications of collapsible tube flows, and to Bertram (2003) for a review of experimental studies of flows in the Starling resistor.

The review paper by Heil & Jensen (2003) provides an overview of early theoretical models of flows in collapsible tubes. Most of these were either based on simplified one-dimensional analyses that involve a large number of *ad hoc* approximations, or were computational studies of the corresponding two-dimensional system – a collapsible channel in which part of one of the sidewalls is replaced by a pre-stressed elastic membrane (e.g. Luo & Pedley 1996, 1998; Luo *et al.* 2008; Liu *et al.* 2009). Self-excited oscillations in collapsible channel flows were also considered by Jensen & Heil (2003), who employed asymptotic techniques to derive explicit predictions for the critical Reynolds number at which self-excited oscillations first develop. Their asymptotic analysis applies in a parameter regime in which the wall tension is so large that the wall performs a high-frequency oscillation which drives a large-Strouhal-number oscillatory flow in the channel. The analysis identified a simple mechanism by which the oscillating wall can extract energy from the mean flow. Assuming that the wall performs oscillations with a ‘mode 1’ axial mode shape (characterized by a single extremum in the displacement near the middle of the elastic segment, as sketched in figure 2), the oscillatory wall motion periodically displaces some of the fluid in the collapsible section and thus generates oscillatory axial ‘sloshing flows’ in the rigid upstream and downstream sections. Heil & Jensen (2003) decomposed the flow field \mathbf{u}^* into its mean, $\bar{\mathbf{u}}^*$, and a time-periodic perturbation $\hat{\mathbf{u}}^* = (\hat{u}^*, \hat{v}^*)$. They then showed that, in the parameter regime considered, $\hat{\mathbf{u}}^*$ is governed by a balance between

unsteady axial fluid inertia, $\rho \partial \hat{u}^* / \partial t^*$, and the axial pressure gradient, $\partial \hat{p}^* / \partial x^*$, resulting in a blunt velocity profile in the core of the channel, with thin Stokes layers near the wall. The sketch in figure 2 correctly suggests that the sloshing flows in the upstream and downstream sections will generally have different amplitudes. For instance, if the downstream rigid section is much longer than the upstream one, most of the fluid is displaced into the upstream segment since it offers less viscous and inertial resistance to the flow. The key observation made by Jensen & Heil (2003) is that the oscillatory sloshing flows generate an influx/outflux of kinetic energy at the upstream/downstream ends of the system. If the amplitude of the sloshing flows at the upstream end exceeds that at the downstream end, the sloshing flows therefore create a net influx of kinetic energy into the system. If this exceeds the additional losses associated with the oscillatory flows (primarily, the additional losses due to the viscous dissipation in the Stokes layers) the system can extract energy from the mean flow, allowing the oscillations to grow in amplitude. Heil & Jensen (2003) demonstrated excellent agreement between their theoretical predictions and direct numerical simulations for large wall tensions. Furthermore, even the large-amplitude limit-cycle oscillations that developed in channels with relatively small wall tensions showed good qualitative agreement with the theoretical predictions, even though the frequency of the oscillation was not particularly large. Even oscillations with Strouhal numbers as low as $St \approx 0.05$ still behaved essentially as predicted by the large-Strouhal-number theory.

Heil & Waters (2006) showed that, while the instability mechanism identified by Jensen & Heil (2003) is, in principle, independent of the spatial dimension, it is unlikely to be able to explain the development of self-excited oscillation in initially axisymmetric (or weakly buckled) three-dimensional collapsible tubes. This is because the change in tube volume induced by the slight non-axisymmetric buckling of an initially axisymmetric tube (with displacement amplitude of $O(\epsilon)$) only induces volume changes of size $O(\epsilon^2)$. Hence the axial sloshing flows induced by the oscillatory wall motion are much weaker than in the corresponding two-dimensional system where an $O(\epsilon)$ wall deflection generates $O(\epsilon)$ sloshing flows. Heil & Waters (2006) showed that in three-dimensional axisymmetric tubes of moderate length, the flow induced by the small-amplitude non-axisymmetric buckling of the tube wall is, in fact, dominated by the transverse flows that develop within the tube's cross-sections. Furthermore, to leading order in the displacement amplitude, the transverse flows do not interact with the axial mean flow. The system can therefore not extract any energy from the mean flow and the inevitable viscous losses ultimately cause the oscillations to decay. Heil & Waters (2006) performed numerical simulations of these decaying oscillations, restricting themselves to a study of the two-dimensional transverse flows within the cross-sections of an elastic tube, modelling the elastic boundary of the cross-section as an elastic ring. The simulations showed that decaying non-axisymmetric 'Type B' oscillations, illustrated in figure 3(b), switch to a 'Type A' oscillation, illustrated in figure 3(a), before approaching their ultimate non-axisymmetrically buckled equilibrium configuration. Heil & Waters (2006) conjectured that the reverse transition may occur when self-excited oscillations develop from non-axisymmetrically buckled equilibrium configurations of three-dimensional collapsible tubes. They argued that, following the onset of the oscillations, the tube wall will initially have to perform small-amplitude 'Type A' oscillations about the buckled equilibrium configuration. Once the amplitude of these oscillations has grown sufficiently, the system may be able to cross the axisymmetric state and overshoot into a configuration in which the cross-section's major and minor half-axes are reversed, as in a 'Type B' oscillation.

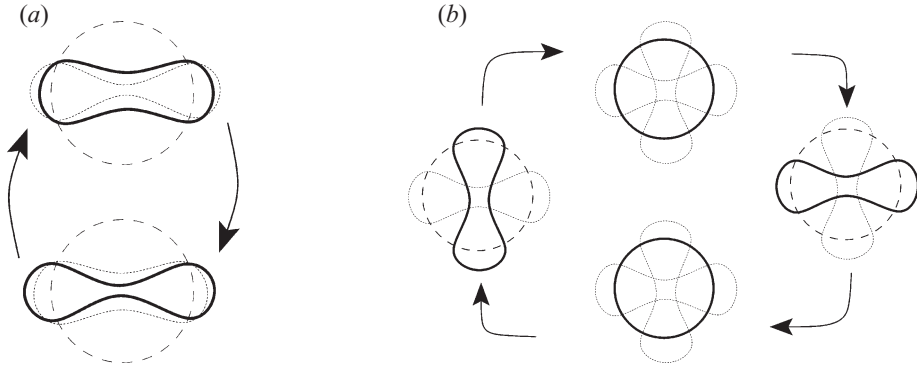


FIGURE 3. Sketch of the tube's cross-sections during (a) 'Type A' and (b) 'Type B' oscillations. The dashed lines indicate the undeformed axisymmetric cross-sections, the dotted lines represent the most strongly deformed configurations during the oscillation.

(Note that in Heil & Waters 2006 the 'Type A/B' oscillations were referred to as 'Type II/I', respectively. We changed their enumeration here to reflect the order in which the two types of oscillation arise during the onset of self-excited oscillations, while avoiding a direct conflict in notation.)

Since the instability mechanism identified by Jensen & Heil (2003) relies on the energetics of the sloshing flows, Heil & Waters (2008) analysed the energy budget of flows in oscillating collapsible tubes whose walls perform prescribed motions with period \mathcal{T}^* and a prescribed mode shape that resembled the eigenmodes of an oscillating elastic tube. They demonstrated that, provided the magnitude of the sloshing flows at the upstream end exceeds that at the downstream end, the wall begins to extract energy from the flow when the mean flow exceeds a critical value. However, in line with the predictions of Heil & Waters (2006), the extraction of energy was found to work efficiently only if the tube performed oscillations about a buckled mean configuration. Heil & Waters (2008) postulated that in an elastic tube the flow rate beyond which the wall extracts energy from the flow corresponds to the flow rate beyond which the oscillations would grow in amplitude. Assuming that the period of the oscillation \mathcal{T}^* is set by a dynamic balance between fluid inertia and the wall's bending stiffness K , so that $\mathcal{T}^* \sim a\sqrt{\rho/K}$, where a and ρ are the undeformed tube radius and the fluid density, respectively, Heil & Waters (2008) employed scaling arguments to predict that the critical Reynolds number for the onset of self-excited oscillations should scale like

$$Re_{crit} = \frac{\rho a U_{crit}}{\mu} \sim \sqrt{\frac{a}{\mu} \sqrt{\rho K}}, \quad (1.1)$$

where μ is the dynamic viscosity of the fluid, and the Reynolds number is formed with the mean velocity of the flow. This scaling was recently confirmed (again for the case of prescribed wall motion) by Whittaker *et al.* (2010*a,b*), using asymptotic methods.

In the present paper we finally explore the onset of self-excited oscillations in three-dimensional collapsible tubes with full coupling between the fluid and solid mechanics, using the insight gained from our previous studies to identify regions of parameter space in which the onset of self-excited oscillations is most likely. We follow the growing oscillations into the large-amplitude regime and assess to what extent the system's behaviour agrees with our previous predictions and conjectures.

2. The model

We consider the unsteady finite-Reynolds-number flow of a viscous fluid (density ρ and viscosity μ) through a collapsible tube of undeformed radius a and length L^* , mounted on two rigid tubes of lengths L_{up}^* and L_{down}^* , respectively, as shown in figure 1. The total length of the tube is $L_{total}^* = L_{up}^* + L^* + L_{down}^*$. (Throughout this paper, asterisks are used to distinguish dimensional quantities from their non-dimensional equivalents.) Since the influx of kinetic energy is maximized when the velocity fluctuations are suppressed at the outflow, we drive the flow by imposing a constant flow rate, $\dot{V}^* = \dot{V}_0^*$, at the end of the downstream rigid tube. (We note that this set-up differs from that employed in most existing collapsible tube experiments where the flow tends to be driven by an applied pressure drop. However, we believe that, in principle, our boundary condition could be realized experimentally by driving the flow with a volumetric pump, attached to the far downstream end of the system.) At the inlet we impose parallel inflow and subject the flow to zero axial traction. In the absence of any wall deformation, the flow is therefore steady Poiseuille flow.

We model the tube as a thin-walled elastic shell of thickness h , Young's modulus E and Poisson ratio ν , loaded by an external pressure p_{ext}^* and by the traction that the fluid exerts on its inside. The shell is assumed to be clamped to the rigid upstream and downstream tubes.

We non-dimensionalize all lengths with the undeformed tube radius, a , the fluid velocity with $U = \dot{V}_0^*/a^2$, and the fluid pressure on the associated viscous scale, so that $p^* = (\mu U/a) p$. Time is non-dimensionalized on the flow's intrinsic time scale so that $t^* = (a/U)t$. We parametrize the non-dimensional position vector to the undeformed tube wall by two Lagrangian coordinates (ξ_1, ξ_2) as

$$\mathbf{r}_w = (\cos(\xi_2), \sin(\xi_2), \xi_1)^T, \quad (2.1)$$

written here with respect to a Cartesian coordinate system (x_1, x_2, x_3) , where $\xi_1 \in [0, L_{total}]$ and $\xi_2 \in [0, 2\pi]$. The same Lagrangian coordinates are used to write the time-dependent position vector to the deformed tube wall as $\mathbf{R}_w(\xi_1, \xi_2, t)$.

The flow is then governed by the non-dimensional Navier–Stokes equations

$$Re \left(\frac{\partial \mathbf{u}}{\partial t} + \mathbf{u} \cdot \nabla \mathbf{u} \right) = -\nabla p + \nabla^2 \mathbf{u}, \quad \nabla \cdot \mathbf{u} = 0, \quad (2.2)$$

subject to the no-slip conditions

$$\mathbf{u} = \frac{\partial \mathbf{R}_w}{\partial t} \quad \text{on the wall.} \quad (2.3)$$

The assumption of parallel, axially traction-free inflow implies

$$p = u_1 = u_2 = 0 \quad \text{at } x_3 = 0. \quad (2.4)$$

At the outflow we impose parallel flow with the required flow rate by setting

$$u_1 = u_2 = 0 \quad \text{and} \quad \int u_3 \, dA = \dot{V}_0 = \pi \quad \text{at } x_3 = L_{total}. \quad (2.5)$$

We describe the deformation of the tube wall by large-displacement (geometrically nonlinear) thin-shell theory, using a linear constitutive equation (Hooke's law) because non-axisymmetric buckling of thin-walled elastic tubes only induces small strains. We

non-dimensionalize all solid mechanics stresses on the tube's bending stiffness:

$$K = \frac{E}{12(1-\nu^2)} \left(\frac{h}{a}\right)^3. \quad (2.6)$$

The position vector to the deformed tube wall is then determined by the principle of virtual displacements,

$$\begin{aligned} \int_0^{2\pi} \int_0^L E^{\alpha\beta\gamma\delta} \left(\gamma_{\alpha\beta} \delta\gamma_{\gamma\delta} + \frac{1}{12} \left(\frac{h}{a}\right)^2 \kappa_{\alpha\beta} \delta\kappa_{\gamma\delta} \right) d\xi_1 d\xi_2 \\ = \frac{1}{12} \left(\frac{h}{a}\right)^2 \int_0^{2\pi} \int_0^L \mathbf{f} \cdot \delta \mathbf{R}_w \sqrt{A} d\xi_1 d\xi_2, \end{aligned} \quad (2.7)$$

where $\gamma_{\alpha\beta}$ and $\kappa_{\alpha\beta}$ are the mid-plane strain and bending tensors, respectively, and $E^{\alpha\beta\gamma\delta}$ is the fourth-order tensor of elastic constants. The components of the load vector \mathbf{f} are given by

$$f_i = p_{ext} N_i - Q \left(p N_i - \left(\frac{\partial u_i}{\partial x_j} + \frac{\partial u_j}{\partial x_i} \right) N_j \right), \quad (2.8)$$

where

$$Q = \frac{\mu U}{aK}, \quad (2.9)$$

and the N_i are the component of the outer unit normal.

For a fixed tube geometry, the problem is therefore governed by three main non-dimensional parameters,

$$Re = \frac{\rho a U}{\mu}, \quad Q = \frac{\mu U}{aK} \quad \text{and} \quad p_{ext}, \quad (2.10)$$

which represent the ratio of the fluid's inertial and viscous stresses, the ratio of the fluid's viscous stresses to the wall stiffness and the ratio of the external pressure to the wall stiffness, respectively. To facilitate the interpretation of the results, we wish to interpret the Reynolds number Re as a measure of the flow rate through the tube. Following Hazel & Heil (2003), we will therefore perform parameter studies in which the material parameter

$$H = \frac{Re}{Q} = \frac{\rho a^2 K}{\mu^2} \quad (2.11)$$

is kept constant. For a given value of Re , the parameter Q then follows from $Q = Re/H$. The large wall stiffnesses required to obtain high-frequency oscillations can be realized by setting H to a sufficiently large value.

3. Discretization

We discretized the governing equations using Heil & Hazel's object-oriented multi-physics finite-element library `oomph-lib` (Heil & Hazel 2006), available as open-source software at <http://www.oomph-lib.org>. In typical experiments the collapsible tube tends to buckle in a two-lobed mode. Therefore we discretized only a quarter of the domain, $x_1, x_2 \geq 0$ and applied appropriate symmetry conditions in the planes $x_1 = 0$ and $x_2 = 0$. The arbitrary Lagrangian–Eulerian form of the Navier–Stokes equations was discretized with hexahedral Taylor–Hood (Q2Q1) elements on a body-fitted mesh, using `oomph-lib`'s algebraic node update procedure to adjust the fluid mesh in

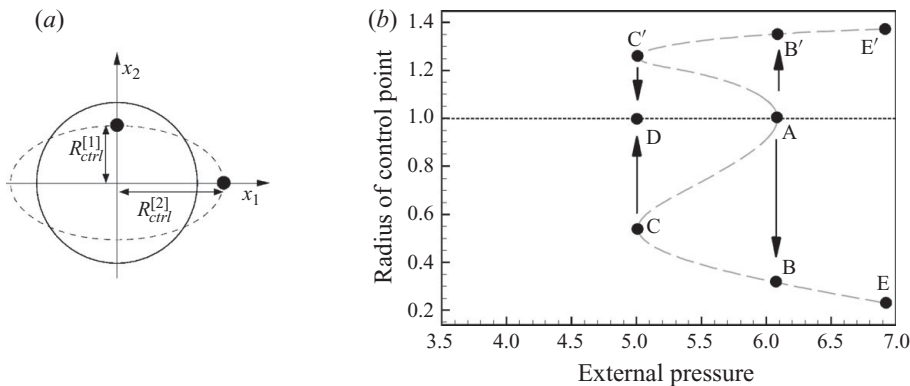


FIGURE 4. (a) Sketch illustrating the radii of the control points used to characterize the tube's deformation. (b) The tube's steady load-displacement diagram in the absence of fluid-structure interaction for $L = 10$, $\nu = 0.49$, $h/a = 1/20$.

response to the changes in the wall shape. The flux constraint (2.5) was incorporated by treating the outflow pressure as an unknown and adding (2.5) to the governing equations. The principle of virtual displacements was discretized with quadrilateral Hermite elements. Steady simulations were performed with a displacement-control technique, imposing the degree of collapse by prescribing the radial displacement of a control point on the tube wall and regarding the external pressure required to achieve this deformation as an unknown. This allowed us to compute the complicated load-displacement curves for the short tubes (shown in figure 5) for which the axisymmetric configuration loses its stability via a subcritical bifurcation. The time-integration was performed with an adaptive second-order BDF scheme (see e.g. Gresho & Sani 2000). The discretized fluid and solid equations were coupled monolithically and the large system of nonlinear algebraic equations to be solved at every time step of the implicit time-integration procedure was solved by *oomph-lib*'s Newton solver. GMRES, preconditioned by *oomph-lib*'s FSI preconditioner (Heil, Hazel & Boyle 2008), was used to solve the linear systems arising in the course of the Newton iteration. Selected runs were performed with various spatial and temporal resolutions to confirm the mesh- and time-step-independence of the results (see figures 11, 14 and 15 and the Appendix).

4. Results

4.1. Short tubes

We start by studying the development of self-excited oscillations in the relatively short collapsible tubes (of length $L = 10$, wall thickness $h/a = 1/20$ and Poisson ratio $\nu = 0.49$) that were analysed in the steady computations by Hazel & Heil (2003). We set the lengths of the upstream and downstream rigid tubes to $L_{up} = 1$ and $L_{down} = 8$, respectively, and keep the material parameter H at a constant value of $H = 10^4$. We explore the tube's behaviour at various Reynolds numbers, using the external pressure, p_{ext} , to control its collapse. Throughout this paper we characterize the tube's deformation by plotting the radii, $R_{ctrl}^{[1]}$ and $R_{ctrl}^{[2]}$, of two material control points that are located in the tube's horizontal and vertical symmetry planes, half-way along the elastic segment (see figure 4a).

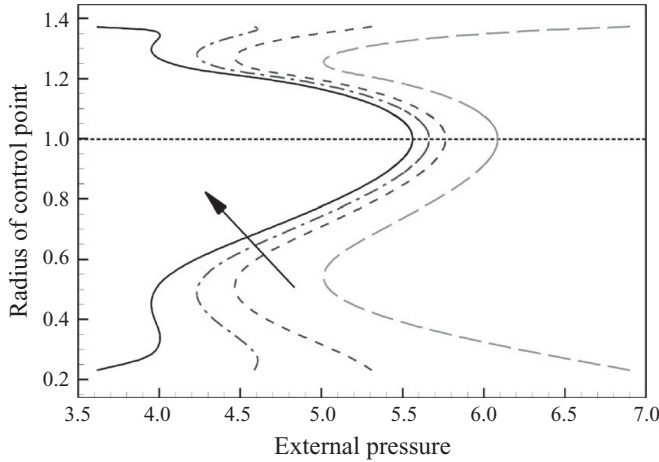


FIGURE 5. The tube's steady load-displacement diagram for $Re = 65, 85, 105$ (increasing in the direction of the arrow) for a tube of length $L = 10$ and $H = 10^4$. The long-dashed line shows the load-displacement diagram in the absence of any fluid-structure interaction. $L_{up} = 1$, $L_{down} = 8$, $\nu = 0.49$, $h/a = 1/20$.

4.1.1. Steady solutions

To explain the tube's steady load-displacement characteristics, we start by considering its behaviour in the absence of any flow. For sufficiently small (or negative) values of p_{ext} , the tube is slightly compressed (or inflated) and it deforms axisymmetrically, so that $R_{ctrl}^{[1]} = R_{ctrl}^{[2]}$. In this mode, the tube is very stiff and large changes in p_{ext} are required to induce even small changes in the tube shape. In the load-displacement diagram shown in figure 4(b) this regime is represented by the nearly straight dotted line of small negative slope. When the external pressure exceeds a critical value of $p_{ext} = p_{ext}^{[buckl]} = 6.09$ (point A), the axisymmetric configuration becomes statically unstable and the tube buckles non-axisymmetrically. (The buckling pressure is about twice as large as that of an infinitely long tube (or a ring) because the clamped ends of the finite-length tube provide additional structural support.) The loss of stability occurs via a subcritical bifurcation and for $p_{ext} > p_{ext}^{[buckl]}$, the tube's only statically stable equilibrium configurations are strongly buckled tube shapes, represented by the branches B-E (B'-E'), along which $R_{ctrl}^{[1]} < 1$ and $R_{ctrl}^{[2]} > 1$. (Note that exchanging $R_{ctrl}^{[1]}$ and $R_{ctrl}^{[2]}$ corresponds to a simple rigid-body rotation of the tube by 90° .) In this regime an increase in p_{ext} continuously increases the tube's collapse. A reduction in p_{ext} reopens the tube until the statically stable non-axisymmetric solution branch disappears at the limit point C (C') where $p_{ext} = 5.01$. The branch C-A (C'-A) represents statically unstable non-axisymmetric equilibria.

Figure 5 illustrates how the fluid flow affects the system's steady behaviour by plotting the tube's load-displacement characteristics at three Reynolds numbers ($Re = 65, 85$ and 105 , increasing in the direction of the arrow; the long-dashed curve corresponds to the case without fluid flow). Since the fluid pressure is kept constant at the tube's far upstream end (see (2.4)), the pressure drop required to drive the viscous flow is generated by a negative pressure at the tube's far downstream end. The presence of the flow therefore reduces the (internal) fluid pressure, and for a given value of p_{ext} , a fluid-conveying tube is subject to a larger compressive load than a tube without any through-flow. Hence in the presence of flow, a smaller value of p_{ext} is required to compress the tube sufficiently to induce its non-axisymmetric

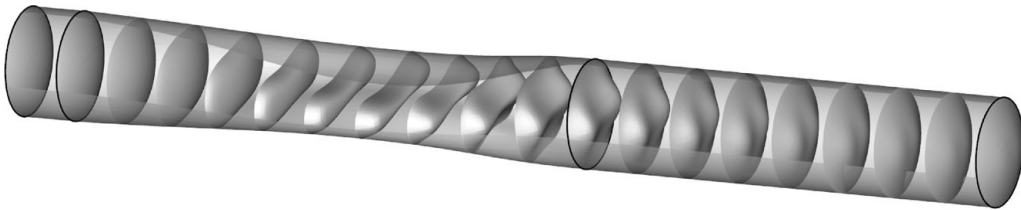


FIGURE 6. Steady flow field in a strongly collapsed tube ($R_{ctrl}^{[1]} = 0.25$) at a Reynolds number of $Re = 105$. The plot shows $3/4$ of the tube wall and profiles of the axial velocity. The direction of the flow is from left to right. The thick solid lines indicate the ends of the rigid tubes. $L = 10$, $L_{up} = 1$, $L_{down} = 8$, $\nu = 0.49$, $h/a = 1/20$ and $H = 10^4$.

buckling. This effect is enhanced at larger flow rates (Reynolds numbers) since an increased flow rate increases the viscous pressure drop along the tube. This explains why $p_{ext}^{[buckl]}$ decreases with an increase in Reynolds number.

Once the tube has buckled non-axisymmetrically, the reduction in its cross-sectional area increases the viscous flow resistance, requiring an even larger pressure drop along the tube to maintain the imposed flow rate. Furthermore, the collapse increases the axial velocity in the collapsed region which leads to a further local reduction in fluid pressure due to the Bernoulli effect. Both effects are strongly destabilizing in the sense that an increase in the tube's collapse increases the compressive load on the tube wall yet further. At sufficiently large Reynolds numbers this creates a second limit point in the load-displacement curve beyond which the flow-induced increase in the compressive load on the wall exceeds the increase in the elastic restoring forces. Over the range of deformations considered in figure 5, no statically stable non-axisymmetric steady solutions exist beyond this point. (It is possible that, in an experiment, the occurrence of opposite wall contact when the tube collapses yet further may increase the tube stiffness sufficiently to restabilize the system; however, such states are beyond the scope of this study.) With a further increase in the Reynolds number the small region in which statically stable buckled solutions exist disappears altogether.

Figure 6 shows a plot of the flow field (three quarters of the tube wall and profiles of the axial velocity) in a strongly collapsed tube at a Reynolds number of $Re = 105$. The increase in the axial velocity in the most strongly collapsed cross-section, responsible for the destabilizing compression via the Bernoulli effect, is clearly visible. The velocity profiles downstream of the most strongly collapsed cross-section show first signs of the two 'jets' that were discussed in more detail by Hazel & Heil (2003). However, at this relatively low Reynolds number, transverse diffusion of momentum returns the flow towards a Poiseuille profile over a few diameters.

4.1.2. Unsteady solutions

We will now investigate the temporal stability of the solutions using the following procedure: we use a steady solution for a certain external pressure as the system's initial condition at $t = 0$. For $t > 0$, we change p_{ext} and compute the system's time-dependent response to this perturbation. We focus on the stability of the non-axisymmetrically buckled steady states since Heil & Waters (2006) predict these to be most susceptible to the instability mechanism described in § 1. (The results presented below will confirm that the axisymmetric configuration tends to be temporally stable, as anticipated.)

Figure 7 illustrates the system's evolution for a range of Reynolds numbers. In each case we used an initial condition for which $R_{ctrl}^{[1]}(t = 0) = 0.375$; for $t > 0$ we set the external pressure to the value required to hold the tube in the adjacent equilibrium

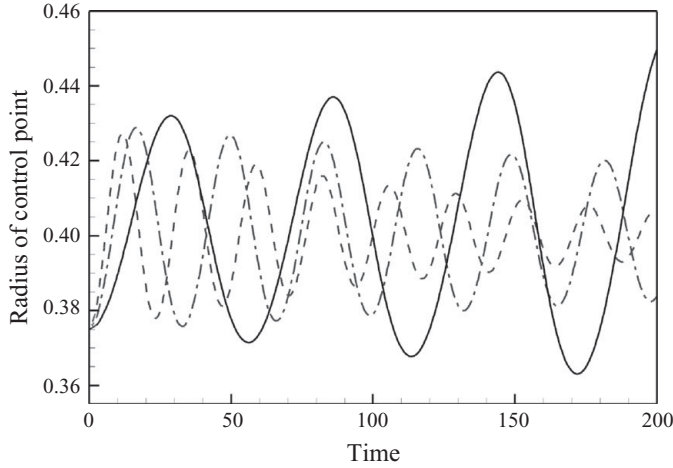


FIGURE 7. Evolution of the control radius $R_{ctrl}^{[1]}$ for $Re = 85$ (dashed), 95 (dash-dotted) and 105 (solid). In all cases the steady solution for $R_{ctrl}^{[1]} = 0.375$ was used as the initial condition at $t = 0$. For $t > 0$ we set p_{ext} to the value that corresponds to the equilibrium state with $R_{ctrl}^{[1]} = 0.4$. $L = 10$, $L_{up} = 1$, $L_{down} = 8$, $\nu = 0.49$, $h/a = 1/20$ and $H = 10^4$.

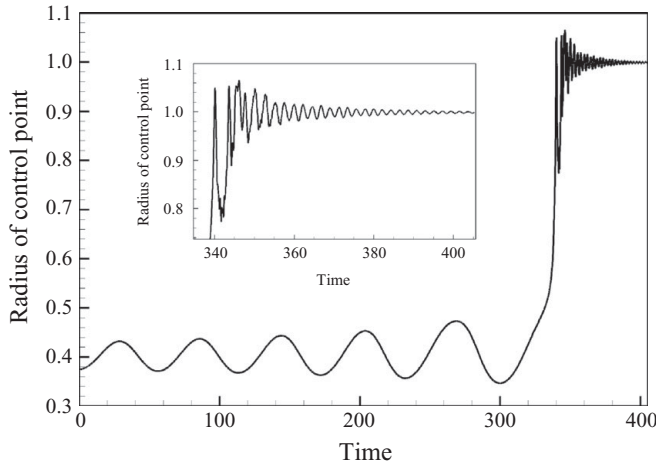


FIGURE 8. Evolution of the control radius $R_{ctrl}^{[1]}$ for $Re = 105$. $L = 10$, $L_{up} = 1$, $L_{down} = 8$, $\nu = 0.49$, $h/a = 1/20$ and $H = 10^4$.

configuration for which $R_{ctrl}^{[1]} = 0.4$. (We note that each computation inevitably starts from a slightly different initial configuration since the steady solution whose stability we wish to investigate does itself depend on the Reynolds number. However, in all cases considered, both equilibrium configurations were statically stable.) For small Reynolds numbers the system performs decaying ‘Type A’ oscillations about the new equilibrium configuration. An increase in the Reynolds number increases the period of the oscillation and decreases the decay rate. For $Re = 105$ the oscillation grows in amplitude, indicating that the static equilibrium configuration has become unstable via a Hopf bifurcation.

Figure 8 follows the growing oscillation for the $Re = 105$ case into the large-amplitude regime. Initially the tube continues to perform growing ‘Type A’ oscillations

about the non-axisymmetric equilibrium configuration corresponding to $R_{ctrl}^{[1]} = 0.4$. As the amplitude of the oscillation increases, the system comes closer and closer to the axisymmetric configuration whenever it passes through its least collapsed state. The character of the oscillation changes dramatically at $t \approx 335$, when the oscillation becomes entrained by the statically stable axisymmetric state. Following the decay of the complex initial transients between $340 \lesssim t \lesssim 360$, the tube wall performs high-frequency damped ‘Type B’ oscillations about the axisymmetric equilibrium configuration.

This behaviour is consistent with the observation by Heil & Waters (2006) that small-amplitude ‘Type B’ oscillations about the axisymmetric configuration only displace very small volumes of fluid from the collapsible section. Since the period of the oscillations is set by a dynamic balance between unsteady fluid inertia and the wall stiffness, the frequency increases dramatically when the system switches to a ‘Type B’ oscillation, following which a much smaller mass of fluid is involved in the oscillation. Furthermore, the reduction in the amplitude of the sloshing flows reduces the influx of kinetic energy to such an extent that the oscillations decay, as predicted. We note that the transition from a growing oscillation about a collapsed configuration to a decaying oscillation about the system’s axisymmetric state is reminiscent of the behaviour displayed by the lumped-parameter model by Bertram & Pedley (1982) (see e.g. figure 8 in that paper), though their simulations employed different boundary conditions.

We performed a large number of additional computations for this tube geometry but were not able to identify any cases for which the system performed sustained large-amplitude limit-cycle oscillations. Following the onset of self-excited oscillations, the tube either reopened towards an axisymmetric configuration (following which the oscillations decayed as in figure 8), or it underwent a catastrophic collapse towards a configuration with opposite wall contact which cannot be resolved with our current computational set-up.

4.2. Long tubes

The non-existence of large-amplitude limit-cycle oscillations for the tube considered in the previous section is due to the fact that (i) the axisymmetric state loses its stability to non-axisymmetric perturbations via a subcritical bifurcation, and (ii) fluid–structure interaction is strongly destabilizing and reduces the range of external pressures over which statically stable non-axisymmetrically buckled solutions exist to a regime in which the corresponding axisymmetric state is still statically stable. Any growing oscillations that arise from the statically stable buckled equilibria therefore ultimately become entrained by the stable axisymmetric solution. The development of sustained self-excited oscillations is therefore likely to be encouraged by changes to the system parameters which (i) change the character of the steady bifurcation from subcritical to supercritical, and (ii) reduce the destabilizing feedback from the fluid–structure interaction. Approach (i) may be achieved by subjecting the tube to a large axial tension and/or by increasing its length; (ii) may be achieved by increasing the wall stiffness via an increase in H . Here, we combine both approaches by increasing the length of the elastic segment to $L = 20$ and increasing H from 10^4 to 10^5 .

4.2.1. Steady solutions

The load-displacement diagram in figure 9 confirms that the change in the problem parameters has the desired effect. The increase in tube length changes the character of the bifurcation so that buckling now occurs via a supercritical bifurcation, regardless

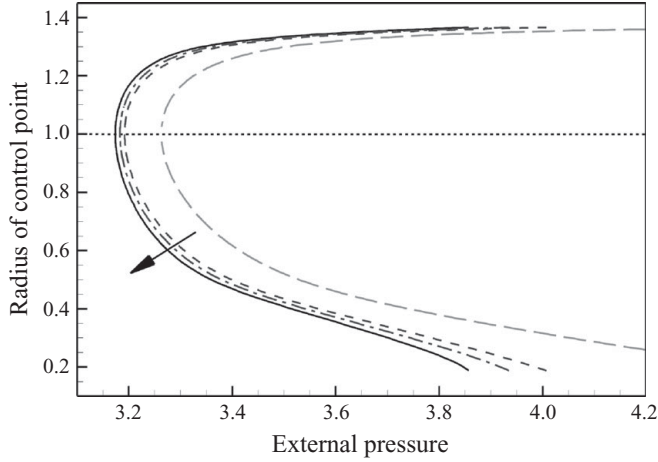


FIGURE 9. The tube's steady load-displacement diagram for $Re = 80, 90, 100$ (increasing in the direction of the arrow) for a tube of length $L = 20$ and $H = 10^5$. The long-dashed line shows the load-displacement diagram in the absence of any fluid-structure interaction. $L_{up} = 1$, $L_{down} = 8$, $\nu = 0.49$ and $h/a = 1/20$.

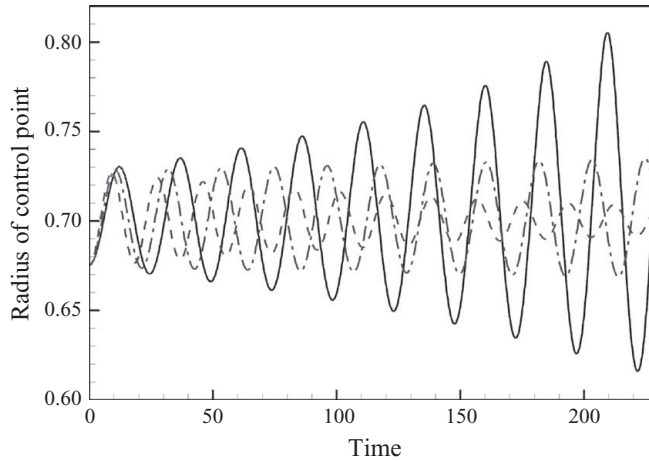


FIGURE 10. Evolution of the control radius $R_{ctrl}^{[1]}$ for $Re = 80$ (dashed), 90 (dash-dotted) and 100 (solid). In all cases the steady solution for $R_{ctrl}^{[1]} = 0.675$ was used as the initial condition at $t = 0$. For $t > 0$ we set p_{ext} to the value that corresponds to the equilibrium state with $R_{ctrl}^{[1]} = 0.7$. $L = 20$, $L_{up} = 1$, $L_{down} = 8$, $\nu = 0.49$, $h/a = 1/20$ and $H = 10^5$.

of the presence or absence of fluid flow. The increase in H reduces the destabilizing feedback from the fluid-structure interaction in the large-displacement regime to such an extent that all post-buckled steady solution branches shown in figure 9 are statically stable.

4.2.2. Unsteady solutions

Figure 10 shows the results of time-dependent simulations performed using the same procedure as in §4.1.2. Here we used the steady solution in which the radius of the control point has a value of $R_{ctrl}^{[1]} = 0.675$ as the initial condition, and for $t > 0$ set p_{ext} to the value required to reopen the tube to $R_{ctrl}^{[1]} = 0.7$. As before, the system performs

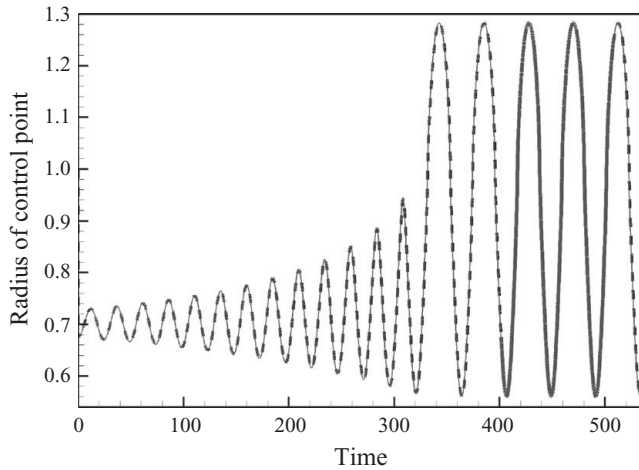


FIGURE 11. Evolution of the control radius $R_{ctrl}^{[1]}$ for $Re = 100$. The dashed and thick lines show the results of spatial and temporal convergence tests, discussed in the Appendix. $L = 20$, $L_{up} = 1$, $L_{down} = 8$, $\nu = 0.49$, $h/a = 1/20$ and $H = 10^5$.

damped oscillations about the new non-axisymmetric equilibrium configuration when the Reynolds number is sufficiently small. An increase in Reynolds number increases the period of the oscillation and decreases its decay rate until, at a Reynolds number of $Re = 100$, the oscillation grows in amplitude.

Figure 11 follows the evolution of the growing oscillation into the large-amplitude regime. As in the previous case, the system initially performs growing ‘Type A’ oscillation during which the tube oscillates about its non-axisymmetric equilibrium configuration. As the amplitude of the oscillation increases, the system again gets closer and closer to the axisymmetric configuration whenever it reaches its least collapsed state. However, in this case, the axisymmetric configuration is statically unstable and presents a potential energy barrier. Once the system has extracted enough energy from the flow it becomes possible to traverse this barrier, allowing the tube to cross the axisymmetric state into a configuration in which the major and minor axes of the cross-section are reversed. Subsequently, the system rapidly settles into a sustained large-amplitude ‘Type B’ oscillation.

Figure 12 shows representative snapshots of the wall shape and the axial velocity profiles over half a period of the large-amplitude limit-cycle oscillation. Figures 12(a) and 12(e) show the system at the two instants when the wall is close to its most strongly collapsed configuration. At these instants the wall is instantaneously at rest and all cross-sections convey the same volume flux. As a result the axial velocity in the most strongly collapsed cross-sections is strongly increased. The axial mode shape resembles a ‘mode 1’ oscillation, with a (single) minimum of the cross-sectional area developing approximately halfway along the tube. The periodic change in the tube volume generates strong sloshing flows which affect the velocity profiles near the inlet. Overall, the flow field is very smooth (and hence easy to resolve numerically; see the Appendix), with the sharpest velocity gradients arising in the relatively thick Stokes layers generated by the sloshing flows (see also figure 16).

Superficially, the system’s large-amplitude limit-cycle oscillations are remarkably similar to those observed in Jensen & Heil’s (2003) study of self-excited oscillations in two-dimensional collapsible channels. In both systems the wall performs

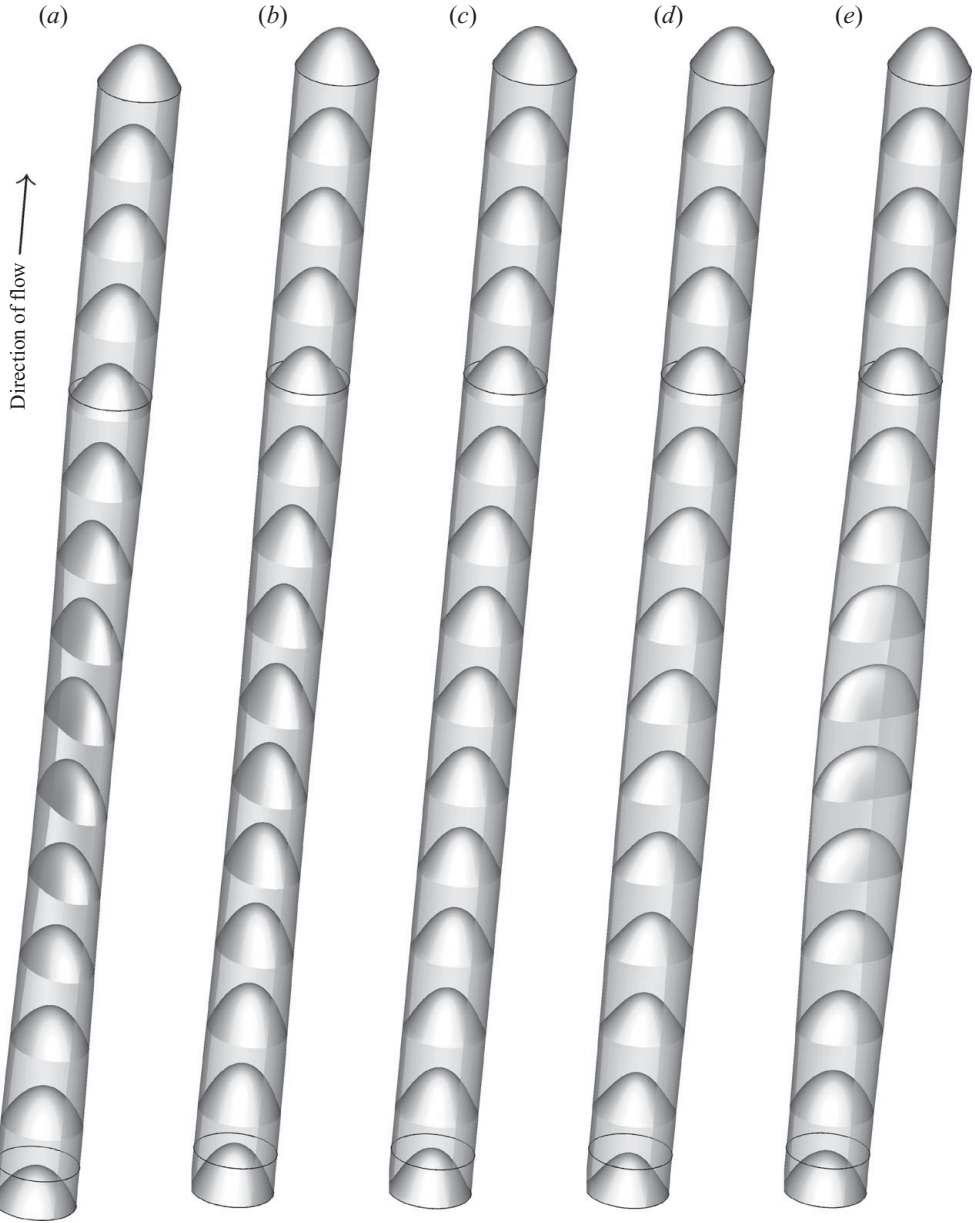


FIGURE 12. Representative snapshots of the flow fields during half a period of the large-amplitude limit-cycle oscillation at a Reynolds number of $Re = 100$. The plots show $3/4$ of the tube wall and profiles of the axial velocity. The thick solid lines indicate the ends of the rigid tubes. (a) $t = 448.00$, (b) $t = 456.59$, (c) $t = 459.30$, (d) $t = 461.60$, (e) $t = 470.23$. $L = 20$, $L_{up} = 1$, $L_{down} = 8$, $\nu = 0.49$, $h/a = 1/20$ and $H = 10^5$.

approximately harmonic large-amplitude ‘mode 1’ oscillations about the undeformed configuration. The details of the oscillations are very different, however. In a two-dimensional channel the extrema of the periodic wall motion are strongly dilated and strongly collapsed channels. The periodic motion of a control point on the channel wall about its undeformed position, with amplitude \mathcal{A} and frequency ω , so that

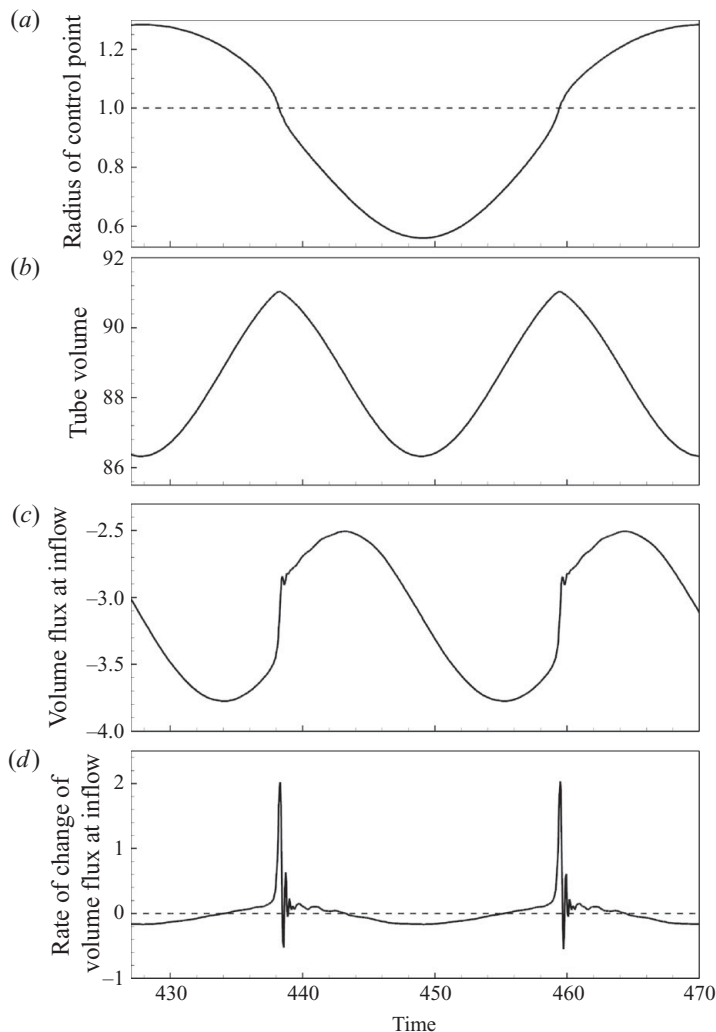


FIGURE 13. Time traces of (a) the radius of the control point, $R_{ctrl}^{[1]}(t)$; (b) the tube volume, $V_{tube}(t)$; (c) the volume flux at the tube's far upstream end, $\dot{V}_{up}(t)$; (d) its rate of change, $d\dot{V}_{up}/dt$, during the large-amplitude limit-cycle oscillation shown in figure 11. The thin dashed lines in (a) and (d) identify the undeformed position of the control point and zero rate of change of volume flux, respectively.

$R_{ctrl}^{[1]} \approx 1 + \mathcal{A} \cos(\omega t)$, therefore generates periodic changes (with frequency ω) in the volume of fluid contained in the channel. At sufficiently high frequency, this generates periodic sloshing flows with a blunt velocity profile (as sketched in figure 2), so that $\hat{u} \sim \mathcal{A} \omega \sin(\omega t)$; these induce large axial pressure gradients, $\partial \hat{p} / \partial x \sim \mathcal{A} \omega^2 \cos(\omega t)$, in phase with the wall motion.

Conversely, in a three-dimensional collapsible tube, the tube volume is minimal twice per period when the tube is in its most deformed configurations (as in figure 12a,e); similarly, the tube attains its maximum volume twice per period, whenever it passes through its approximately axisymmetric configuration where $R_{ctrl}^{[1]} \approx 1$. This is illustrated by the time traces in figure 13. Overall, the motion

of the control point, $R_{ctrl}^{[1]}(t)$, is approximately harmonic and the tube volume, $V_{tube}(t)$, has a sharp peak when $R_{ctrl}^{[1]} \approx 1$. The tube is in one of its two most strongly collapsed configurations when $t \approx 450$. At this instant, the tube attains its minimum volume, the tube wall is at rest, and the volume flux at the upstream end is equal to the mean flow rate, $\dot{V}_{up} = \int \mathbf{u} \cdot \mathbf{n} dA = -\dot{V}_0 = -\pi$ (the flow rate is negative because \mathbf{u} and the outer unit normal, \mathbf{n} , point in opposite directions when the flow enters the tube). As the tube reopens, the magnitude of \dot{V}_{up} increases before rapidly returning to the mean value, $\dot{V}_{up} \rightarrow -\dot{V}_0$ at $t \approx 460$ when $R_{ctrl}^{[1]} \rightarrow 1$. At these instants dV_{tube}/dt vanishes and the axial sloshing flows must be decelerated to zero. This is shown clearly in the plot of the volume flux at the tube's far upstream end, $\dot{V}_{up} = -dV_{tube}/dt$ in figure 13(c). The sudden deceleration of the flow, reflected by the large spike in $d\dot{V}_{up}/dt$, requires a large axial pressure gradient which is generated by a large increase in the fluid pressure at the tube's far downstream end. The sudden pressurization of the approximately axisymmetric tube creates transient high-frequency oscillations during which approximately axisymmetric pressure waves propagate along the tube. The resulting fluctuations in the flow rate at the tube's upstream end are clearly visible in figure 13(c,d).

4.2.3. Relation to the theoretical instability mechanism

The mechanism by which the large-amplitude self-excited oscillations discussed in the previous sections develop are in pleasing qualitative agreement with the predictions made by Heil & Waters (2008). We will now examine the early stages of the self-excited oscillations in more detail to assess if the dependence of their frequency and growth rate on the system parameters is consistent with the scalings that Heil & Waters (2008) derived from an analysis of the system's energy budget. In terms of the non-dimensionalization used in the current paper, their analysis predicts that the non-dimensional period of the oscillation (an inverse Strouhal number) should scale like

$$\mathcal{T} = \frac{\mathcal{F}^* U}{a} = St^{-1} \sim \sqrt{Re} Q = \frac{Re}{\sqrt{H}}, \quad (4.1)$$

while the scaling (1.1) for the Reynolds number at which the system performs energetically neutral oscillations can be expressed in terms of the parameter H as

$$Re_{crit} = \frac{\rho a U_{crit}}{\mu} \sim \sqrt{\frac{a}{\mu} \sqrt{\rho K}} = H^{1/4}. \quad (4.2)$$

We performed a large number of numerical simulations for different values of H , and for Reynolds numbers in the vicinity of Re_{crit} . In each case we simulated approximately ten periods of the system's oscillations which we initiated by the same procedure described in the previous section but with a smaller initial perturbation (starting from a steady configuration at which $R_{ctrl}^{[1]} = 0.69$). The growth rate λ and period \mathcal{T} were determined by a Levenberg–Marquardt fit of $R_{ctrl}^{[1]}(t)$ to the fitting function

$$R_{fit}(t) = \bar{R} + \hat{R} \exp(\lambda t) \cos\left(\frac{2\pi t}{\mathcal{T}} + \phi\right). \quad (4.3)$$

The critical Reynolds number was determined from the condition that $\lambda(Re_{crit}) = 0$.

Figure 14(a) shows the period of the oscillations as a function of the Reynolds number for a range of H values. Over the relatively small range of Reynolds numbers considered for each value of H , the period can be seen to increase approximately linearly with Re , consistent with (4.1). Furthermore, \mathcal{T} decreases with an increase

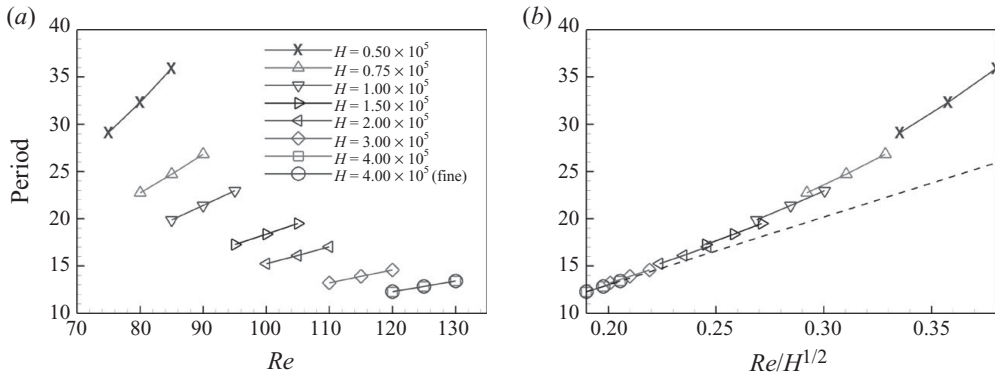


FIGURE 14. (a) The period of the oscillation as function of the Reynolds number for a range of values of H . (b) The same data plotted as a function of $Re/H^{1/2}$. The straight dashed line is an extension of the curve for $H = 4 \times 10^5$. The legend in (a) applies to both figures. The circular markers for $H = 4 \times 10^5$ were obtained from computations with an increased spatial resolution (see the Appendix). $L = 20$, $L_{up} = 1$, $L_{down} = 8$, $\nu = 0.49$ and $h/a = 1/20$.

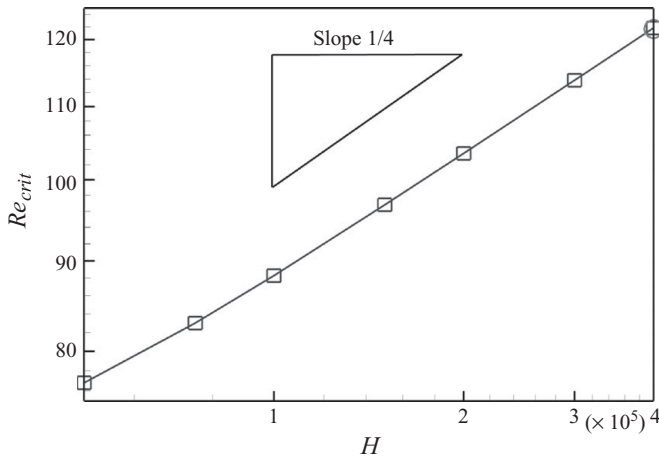


FIGURE 15. The critical Reynolds number as a function of H . The circular marker for $H = 4 \times 10^5$ was obtained from computations with an increased spatial resolution (see the Appendix). $L = 20$, $L_{up} = 1$, $L_{down} = 8$, $\nu = 0.49$ and $h/a = 1/20$.

in the wall stiffness (i.e. an increase in H), which is consistent with the assumption that the oscillations are governed by a balance of unsteady fluid inertia and the wall's elastic restoring forces. However, for the cases considered, the period of the oscillations is not particularly large, and the largest Strouhal number (achieved for $Re = 120$ and $H = 4 \times 10^5$) is just $St = 1/\mathcal{T} = 0.08$. As a result, the plot of the period as a function of Re/\sqrt{H} shown in figure 14(b) deviates slightly from the theoretical prediction, though the scaling becomes increasingly accurate as H (and thus the frequency of the oscillation) increases.

Figure 15 shows a plot of the critical Reynolds number Re_{crit} as a function of H . Again, the agreement with the theoretical prediction, $Re_{crit} \sim H^{1/4}$, is very satisfactory, given the relatively small Strouhal number, and, as for the period, the agreement improves with increasing H .

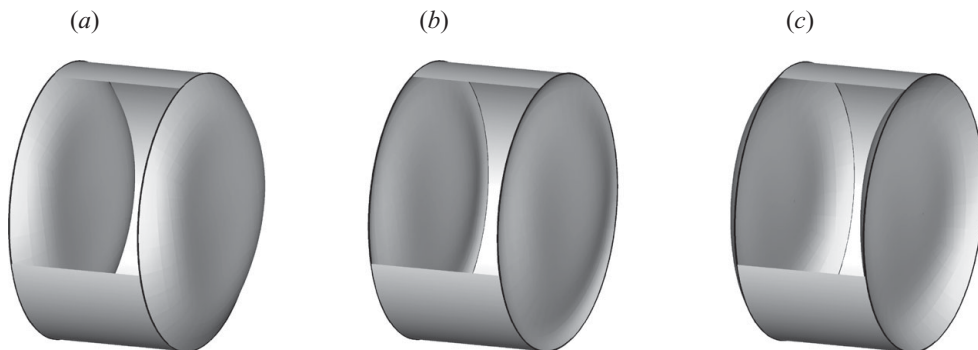


FIGURE 16. Profiles of the axial velocity perturbation in the upstream rigid tube, obtained by subtracting Poiseuille flow from the computed velocity field, at three instants during a small-amplitude oscillation. The direction of the mean flow is from left to right. (a) $t = 30.15$, close to the maximum positive sloshing flow; (b) $t = 33.15$, close to zero sloshing flow; (c) $t = 36.15$, close to the maximum negative sloshing flow. The period of the oscillation is $\mathcal{T} = 12.27$. $Re = 130$, $H = 4 \times 10^5$, $L = 20$, $L_{up} = 1$, $L_{down} = 8$, $\nu = 0.49$ and $h/a = 1/20$.

Given the relatively low Strouhal numbers of the oscillations, it is desirable to assess to what extent the character of the sloshing flows in the computations is consistent with the assumptions of the analysis performed by Heil & Waters (2008); specifically, we wish to establish if the perturbations to the mean flow can indeed be decomposed (at least approximately) into a relatively flat core flow region with Stokes layers near the tube walls. Unfortunately, the extraction of the perturbation velocities from the full flow field is not straightforward. Within the oscillating segment, the tube wall undergoes finite-amplitude motions and it is difficult to define the concept of a mean flow within a spatially varying fluid volume. The fluid volume in the downstream rigid tube is fixed, but, for the boundary conditions employed in our simulations, there are no net sloshing flows. Hence the only part of the fluid domain in which the character of the sloshing flows can be assessed is the upstream rigid tube. Figure 16 shows plots of the axial velocity perturbation $\hat{u}_3 \equiv u_3(x_1, x_2, x_3, t) - 2(1 - x_1^2 - x_2^2)$, obtained by subtracting the Poiseuille flow profile from the instantaneous axial velocity within the upstream rigid tube. The profiles were extracted at three characteristic instants of the oscillation at a Reynolds number of $Re = 130$. The wall performs a ‘Type A’ oscillation with an approximate period of $\mathcal{T} = 12.27$, corresponding to a Strouhal number of $St = 0.08$ and thus a Womersley number of $\alpha^2 = Re St = 10.6$. The profile of the velocity perturbation has the expected structure, with clearly defined Stokes layers whose (relatively large) thickness is well approximated by the classical estimate $\delta_{Womersley} = 1/\alpha = 0.31$. We are therefore confident that the good agreement between the theoretical scaling estimates and the computational results shown in figures 14 and 15 is not fortuitous.

5. Summary and discussion

We have presented what we believe to be the first direct numerical simulation of large-amplitude self-excited oscillations of three-dimensional collapsible tubes. Guided by predictions from previous theoretical and computational studies, we applied boundary conditions that facilitate the onset of self-excited oscillations via the instability mechanism proposed by Jensen & Heil (2003). For sufficiently long

tubes, the system's overall behaviour was found to be in good qualitative agreement with the theoretical predictions, even though in most of the computations the frequency of the oscillations was not particularly high. Specifically, the dependence of the period of the oscillation and the critical Reynolds number on the system parameters was found to be consistent with the scalings found by Heil & Waters (2008) and Whittaker *et al.* (2010*a,b*), which were derived from an analysis of the system's energy budget with prescribed wall motion. Following the onset of the self-excited oscillations (via small-amplitude 'Type A' oscillations about the buckled equilibrium configuration), the amplitude of the oscillation continued to grow until the system was able to traverse the (statically unstable) axisymmetric state. Following this, the system settled into a large-amplitude 'Type B' limit cycle oscillation, in pleasing agreement with Heil & Waters' (2006) conjecture.

In the present paper we only considered two specific tube geometries and showed that the length of the elastic segment can have a strong effect on the large-amplitude oscillations. We note that the tube geometry (including the lengths of the upstream and downstream rigid tubes) also affects the period and growth rate of the initial small-amplitude oscillations, and refer to Whittaker *et al.* (2010*a,b*) for a discussion of these dependencies.

Our computational model was deliberately kept as simple as possible and we only considered the case in which the flow is driven by imposing the volume flux at the far downstream end since this made the system most susceptible to the development of self-excited oscillations via the instability mechanism of Jensen & Heil (2003). We acknowledge that this differs from the typical experimental set-up in which the flow tends to be driven by an applied pressure drop but note that Whittaker *et al.* (2010*a*) demonstrated (at least for the case of prescribed wall motions) that the instability can also arise for pressure-driven flows, provided the difference in the amplitude of the sloshing flows in the upstream and downstream rigid tubes is created by other means, e.g. by having a downstream rigid tube that is longer than its upstream counterpart, as in the two-dimensional computations by Jensen & Heil (2003). However, with such boundary conditions the instability develops at larger Reynolds numbers (since some kinetic energy is lost through the downstream boundary) and, following the onset of neutrally stable oscillations, it takes longer for the system to settle into steady-state oscillations because of transient adjustments to the mean flow. We expect the same behaviour in the fully-coupled case considered here. We wish to reiterate, however, that the instability mechanism identified by Jensen & Heil (2003) will not work if the flow rate is prescribed at the upstream end of the tube (as in the simulations of Luo & Pedley 1996, say), or if the upstream rigid tube is the longer of the two rigid segments. With such boundary conditions, self-excited oscillations may, of course, still develop by other mechanisms.

Since the instability mechanism studied in this paper involves oscillations that are governed by a dynamic balance between fluid inertia and the tube's wall stiffness, wall inertia was not included into our model. This is likely to be justifiable for sufficiently light or thin-walled tubes, though we acknowledge that the inclusion of wall inertia would introduce additional modes into the system. This is because a heavy wall can perform oscillations even in the absence of fluid. It is possible that the presence of these modes gives rise to additional flutter-type instabilities (Miles 1957; Benjamin 1963), as observed, e.g. in the two-dimensional simulations of Luo & Pedley (1996).

The imposition of an exact two-fold symmetry on the flow and wall deformation was motivated by experimental observations which show that the tube tends to buckle

in a two-lobed mode. This allowed a significant reduction in the computational cost, but made it impossible to capture any symmetry breaking bifurcations in the flow that are likely to arise at sufficiently large Reynolds numbers. Whether such secondary instabilities play a role in the development of self-excited oscillations as suggested by Kouanis & Mathioulakis (1999) is still an open question.

The instability mechanism considered here requires the tube to perform oscillations of sufficiently high frequency. In terms of the non-dimensionalization employed in this paper, this requires the material parameter H to be sufficiently large. Using the properties of the rubber tubes used in the experiments by Bertram & Elliot (2003) and Truong & Bertram (2009) ($a = 6.5$ mm, $h = 1$ mm, $\nu = 0.5$ and $E = 3.15$ MPa) and assuming water ($\mu = 10^{-3}$ kg (m s) $^{-1}$ and $\rho = 1000$ kg m $^{-3}$) as the working fluid, yields $H = 5.38 \times 10^7$. This is well in excess of the parameters used in the simulations in this paper, indicating that sufficiently large values of H can easily be realized experimentally. We wish to stress, however, that the character of the flow fields observed during self-excited oscillations in the experiments by Truong & Bertram (2009) with pressure-driven flows differs significantly from those observed in the computations presented here. In particular, the velocity perturbations induced by the wall oscillation were most pronounced in the downstream rigid tube, while the flow field in the upstream rigid tube remained virtually unaffected by the oscillations, suggesting that the oscillations observed in these experiments arise via a different mechanism. While we plan to perform simulations of such oscillations in the near future, we also hope that experimentalists may be sufficiently intrigued by our results to initiate an experimental study using the boundary conditions considered here.

The authors wish to acknowledge many helpful discussions with Sarah Waters, Robert Whittaker, Oliver Jensen, Andrew Hazel and Chris Bertram. The numerical simulations benefited greatly from Richard Muddle's work on `oomph-lib`'s parallel preconditioning framework. The research was supported by a grant from EPSRC.

Appendix. Convergence tests

We performed careful spatial and temporal convergence tests to ensure the mesh and time step independence of our results. The flow field in the long tubes considered in §4.2 was very smooth (see figures 12 and 16) and a fairly coarse spatial resolution involving just 8980 degrees of freedom was sufficient to resolve the flow field. Selected runs were repeated with a much finer spatial resolution involving 67 550 degrees of freedom. The time-integration was performed with at least 160 time steps per period of the oscillation. When analysing the growth rates of the small-amplitude oscillations in §4.2.3, computations were performed with a fixed time step; in all other cases, adaptive time stepping was used to allow the resolution of the higher frequency oscillations that arise whenever the tube approaches the axisymmetric configuration, as in figures 8 or 13.

Results of representative convergence tests are shown in figure 11 where the solid and dashed lines were obtained from computations with the standard spatial resolution, but using different temporal convergence criteria that resulted in average time steps of $\Delta t \approx 0.12$ (solid) and $\Delta t \approx 0.05$ (dashed), respectively. The thick solid line shows the results of a much more costly simulation, performed with the finer spatial resolution. This simulation was restarted from the results obtained with the

standard resolution and a uniform mesh refinement was applied before continuing the time-integration during the system's large-amplitude limit cycle oscillation.

The different markers for the results with $H = 4 \times 10^5$ in figures 14 and 15 show the effect of the spatial refinement on the computed period and growth rate of the oscillations. The square and circular markers represent results obtained on the standard and refined meshes, respectively.

REFERENCES

- BENJAMIN, T. 1963 The threefold classification for unstable disturbances in flexible surfaces bounding inviscid flows. *J. Fluid Mech.* **16**, 436–450.
- BERTRAM, C. D. 2003 Experimental studies of collapsible tubes. In *Flow in Collapsible Tubes and Past Other Highly Compliant Boundaries* (ed. T. J. Pedley & P. W. Carpenter), pp. 51–65. Kluwer.
- BERTRAM, C. D. & ELLIOT, N. S. J. 2003 Flow-rate limitation in a uniform thin-walled collapsible tube, with comparison to a uniform thick-walled tube and a tube of tapering thickness. *J. Fluids Struct.* **7**, 541–559.
- BERTRAM, C. D. & PEDLEY, T. J. 1982 A mathematical model of unsteady collapsible tube behaviour. *J. Biomech.* **15**, 39–50.
- GRESHO, P. & SANI, R. 2000 *Incompressible Flow and the Finite Element Method. Volume Two: Isothermal Laminar Flow*. John Wiley and Sons.
- GROTBERG, J. B. & JENSEN, O. E. 2004 Biofluid mechanics in flexible tubes. *Annu. Rev. Fluid Mech.* **36**, 121–147.
- HAZEL, A. L. & HEIL, M. 2003 Steady finite Reynolds number flow in three-dimensional collapsible tubes. *J. Fluid Mech.* **486**, 79–103.
- HEIL, M. & HAZEL, A. L. 2006 oomph-lib – an object-oriented multi-physics finite-element library. In *Fluid-Structure Interaction* (ed. M. Schäfer & H.-J. Bungartz), pp. 19–49. Springer. oomph-lib is available as open-source software at <http://www.oomph-lib.org>.
- HEIL, M., HAZEL, A. L. & BOYLE, J. 2008 Solvers for large-displacement fluid-structure interaction problems: segregated vs. monolithic approaches. *Comput. Mech.* **43**, 91–101.
- HEIL, M. & JENSEN, O. E. 2003 Flows in deformable tubes and channels – theoretical models and biological applications. In *Flow in Collapsible Tubes and Past Other Highly Compliant Boundaries* (ed. T. J. Pedley & P. W. Carpenter), pp. 15–50. Kluwer.
- HEIL, M. & WATERS, S. 2006 Transverse flows in rapidly oscillating, elastic cylindrical shells. *J. Fluid Mech.* **547**, 185–214.
- HEIL, M. & WATERS, S. 2008 How rapidly oscillating collapsible tubes extract energy from a viscous mean flow. *J. Fluid Mech.* **601**, 199–227.
- JENSEN, O. E. & HEIL, M. 2003 High-frequency self-excited oscillations in a collapsible-channel flow. *J. Fluid Mech.* **481**, 235–268.
- KNOWLTON, F. P. & STARLING, E. H. 1912 The influence of variations in temperature and blood pressure on the performance of the isolated mammalian heart. *J. Physiol.* **44**, 206–219.
- KOUANIS, K. & MATHIOULAKIS, D. S. 1999 Experimental flow study within a self oscillating collapsible tube. *J. Fluids Struct.* **13**, 61–73.
- LIU, H. F., LUO, X. Y., CAI, Z. X. & PEDLEY, T. J. 2009 Sensitivity of unsteady collapsible channel flows to modelling assumptions. *Commun. Numer. Meth. Engng* **25**, 483–504.
- LUO, X. Y., CAI, Z. X., LI, W. G. & PEDLEY, T. J. 2008 The cascade structure of linear stabilities of flow in collapsible channels. *J. Fluid Mech.* **600**, 45–76.
- LUO, X. Y. & PEDLEY, T. J. 1996 A numerical simulation of unsteady flow in a two-dimensional collapsible channel. *J. Fluid Mech.* **314**, 191–225.
- LUO, X. Y. & PEDLEY, T. J. 1998 The effects of wall inertia on flow in a two-dimensional collapsible channel. *J. Fluid Mech.* **363**, 253–280.

- MILES, J. W. 1957 On the generation of surface waves by shear flow. *J. Fluid Mech.* **3**, 185–199.
- TRUONG, N. K. & BERTRAM, C. D. 2009 The flow-field downstream of a collapsible tube during oscillation onset. *Commun. Numer. Meth. Engng* **25**, 405–428.
- WHITTAKER, R. J., HEIL, M., BOYLE, J., JENSEN, O. E. & WATERS, S. L. 2010*a* The energetics of flow through a rapidly oscillating tube. Part 2. Application to an elliptical tube. *J. Fluid Mech.* **648**, 83–121.
- WHITTAKER, R. J., WATERS, S. L., JENSEN, O. E., BOYLE, J. & HEIL, M. 2010*b* The energetics of flow through a rapidly oscillating tube. Part 1. General theory. *J. Fluid Mech.* **648**, 123–153.